



# Global kinetic modeling of rapidly pulsed reductants for lean NO<sub>x</sub> traps: Frequency domain analysis and impact of mass transfer

Amin Reihani<sup>a</sup>, Brent Patterson<sup>b</sup>, John W. Hoard<sup>a</sup>, Galen B. Fisher<sup>b,\*</sup>

<sup>a</sup> Department of Mechanical Engineering, University of Michigan, Ann Arbor, MI, 48109, United States

<sup>b</sup> Department of Chemical Engineering, University of Michigan, Ann Arbor, MI, 48109, United States

## ARTICLE INFO

### Keywords:

Aftertreatment  
Lean NO<sub>x</sub> trap  
Rapid pulsing  
Global kinetic modeling  
Mass transfer limitations

## ABSTRACT

In the Rapidly Pulsed Reductants (RPR) process, also known as Di-Air (Bisaiji et al., 2011 [1]), hydrocarbons are injected in rapid pulses ahead of a lean NO<sub>x</sub> trap (LNT) in order to improve its performance at higher temperatures and space velocities while maintaining a reasonable fuel penalty associated with injecting reductants.

In this study, a 23-step global kinetic model is developed to predict the performance and product selectivity of the RPR process using propylene as the reductant over a wide range of pulsing frequencies, particularly for the temperature range of 450–600 °C. Some of the previous studies, (Bisaiji et al., 2012 [2], Perng et al., 2014 [3]) have suggested a reaction mechanism based on the formation of stable isocyanate (–NCO) intermediates at high temperatures which promote the NO<sub>x</sub> conversion efficiency. However, in this study, we are checking whether a global kinetic model based on the conventional (low frequency) NO<sub>x</sub> storage and reduction mechanism is able to predict the NO<sub>x</sub> conversion improvements at higher pulsing frequencies at high temperatures, where the stability and role of previously proposed intermediates for NO<sub>x</sub> reduction is more questionable.

A wide range of low frequency switching experiments were used to fit the kinetic parameters to the low frequency response of the RPR process. This model was then used to explore the high frequency performance of the RPR process. The kinetic model can predict the increase in NO<sub>x</sub> and propylene conversion as well as the change in selectivity of the reaction products, such as NH<sub>3</sub> and CO, when the pulsing frequency is increased from conventional LNT to optimal RPR frequencies near 1 Hz corresponding to maximum NO<sub>x</sub> conversion (Reihani et al., 2018 [4]). However, in order to predict the behavior of RPR above the optimal frequency, it was required to add a model of axial pulse mixing to the kinetic model.

The model results indicate that the main mechanism for improvement in NO<sub>x</sub> conversion at high frequencies and high temperatures is the more efficient utilization of storage sites. Also, the drop in NO<sub>x</sub> conversion at frequencies higher than the optimal frequency is caused by axial mixing of the reductant pulses. In addition, the model and experimental results provide insights into the importance of washcoat diffusion resistance. Particularly, the NO<sub>x</sub> reduction step with propylene becomes increasingly limited by washcoat diffusion at high temperatures and pulsing frequencies. The agreement between the model and the experimental results provides strong support for using this model to describe the RPR process.

## 1. Introduction

Future vehicular emission and fuel economy regulations are becoming increasingly stringent. Therefore, lean-burn engine technologies are being explored that enable lower fuel consumption over a conventional stoichiometric gasoline engine [5,6]. The traditional three-way catalyst will not perform in oxygen-rich exhaust environment; therefore, lean burn engines require an advanced aftertreatment system to reduce tailpipe NO<sub>x</sub> levels. In heavy-duty applications, Selective Catalytic Reduction (SCR) is usually the preferred emissions

control technology; however, SCR systems are bulky and can be difficult to package in smaller applications. SCR also requires an onboard tank of urea solution (DEF) to be refilled periodically [7]. Lean NO<sub>x</sub> Traps (LNTs) offer manufacturers a more compact emissions reduction solution, and are cost effective for smaller diesel engines (with displacements less than ~2 L); however, their performance needs to be improved at high temperatures and space velocities [8].

The Lean NO<sub>x</sub> Trap (LNT) is a lean NO<sub>x</sub> reduction technology which captures NO<sub>x</sub> during periods of lean engine operation (excess oxygen). The engine must run rich for a brief period to react with and release the

\* Corresponding author.

E-mail address: [gbfisher@umich.edu](mailto:gbfisher@umich.edu) (G.B. Fisher).

<https://doi.org/10.1016/j.apcatb.2019.04.076>

Received 20 September 2018; Received in revised form 16 April 2019; Accepted 22 April 2019

Available online 23 April 2019

0926-3373/ © 2019 Elsevier B.V. All rights reserved.

**Nomenclature**

$u$	Axial flow velocity in monolith channel
$x$	Axial position along monolith channel
$\rho$	Mean density
$p$	Local pressure in monolith channel
$c_i$	Molar concentration of species $i$
$\varphi$	Internal effectiveness factor
$S_i$	Reaction source term of species $i$
$D_i$	Diffusivity of species $i$
$\rho_s$	Density of substrate and washcoat
$c_{p,s}$	Washcoat mean specific heat
$k_s$	Thermal conductivity of solid phase
$h$	Convective heat transfer coefficient in rectangular monolith channel
$\rho_g$	Local gas density
$c_{p,g}$	Local gas specific heat capacity
$T_s$	Local washcoat surface temperature
$T_g$	Local gas phase temperature

$G_A$	Gas/washcoat surface area in the monolith channel
$T_{amb}$	Ambient air temperature around reactor
$h_{amb}$	Heat transfer coefficient of reactor tube with ambient
$S_{ext}$	External surface area of the reactor
$\Delta H_i$	Enthalpy of reaction $i$
$R_i$	Local rate of reaction $i$
$C_{out}$	Molar concentration at outlet
$C_{in}$	Molar concentration at inlet
$\tau_{mix}$	Time constant of mixing for modeling mixing in instrument gas chamber.
$D_{AB}$	Molecular diffusivity of species A in B
$D_{KA}$	Knudsen diffusivity
$D_{Ae}$	Effective diffusivity in washcoat
$M_A, M_B$	Molar mass of species A and B
$R$	Gas constant
$T$	Temperature
$T_{inlet}$	Gas temperature at monolith inlet
$\lambda$	Air-fuel equivalence ratio
$f_r$	Rich fraction of HC pulse

stored NOx with the now-excess reductants in the exhaust stream. Typically, a lean period is around 60–100 s and a rich period is 5–10 s [9]. LNT performance is limited above 400 °C and high space velocities because the storage capacity shrinks with increasing temperature. Furthermore, regeneration periods must become more frequent because of this decreased NOx storage capacity, which increases the fuel penalty [10].

Rapidly Pulsed Reductants (RPR) is one way to improve LNT performance. RPR was introduced by Toyota as "Di-Air" [1]. RPR differs from traditional LNT operation in two ways: the lean/rich cycle times are significantly shorter and hydrocarbon (HC) is injected by a fuel injector directly in front of the catalyst [1]. The auxiliary fuel injector allows the engine to run pseudo-independently of the aftertreatment system, as the lean/rich cycling no longer takes place in-cylinder but immediately upstream of the catalyst. RPR system could increase an LNT's effective high NOx conversion temperature range past 600 °C and to higher space velocities. There has been a disagreement among researchers about the mechanism of NOx conversion improvement at high cycling frequencies. One possible mechanism, proposed by Bisaiji et al. [11] and later by Perng et al. [3], attributes the high NOx conversion efficiency under rapid cycling to formation of stable carbon-containing intermediates on the catalyst surface during pulsed HC injection. They reported that these intermediates are stable at higher temperatures over the first few seconds of the lean period leading to reduction of NOx and improvement in NOx conversion of the LNT at high temperatures and space velocities. Reihani et al. [12] identified that NOx conversion improvement at high cycling frequency occurs in a wide range of reductants including different alkenes (e.g., ethylene, propylene, dodecane) as well as CO. The improvement in NOx conversion with H<sub>2</sub> has also been shown in multiple groups which indicates the reduced importance of stable HC intermediates at high temperatures as the primary mechanism for NOx conversion improvement [12,13]. The improvement in cycle-averaged NOx storage rate at high pulsing frequency was suggested as the primary mechanism for improved NOx conversion [12,13]. In addition, it is necessary to reach net rich feed gas condition during pulsing in order to achieve any sensible NOx conversion with the RPR process. As a result, the gas phase mixing of reductant pulses was shown to significantly affect the performance of RPR at high frequencies [14]. Ting et al. distinguished the two mechanism of NOx conversion improvement to be improved utilization of NOx storage sites as the primary, and formation of HC-intermediates as the secondary reason for enhanced high temperature NOx conversion [13]. They also identified a stronger non-isothermal effect with H<sub>2</sub> specifically at the inlet portion of the catalyst which is the reason for

lower NOx conversion with H<sub>2</sub> compared with a propylene reductant.

Quite a few researchers have contributed to the field of LNT modeling by developing both global and microkinetic models [15–21]. Olsson et al. created an LNT global kinetic model in 2005 [15]. They modeled the catalyst monolith as a plug flow reactor and included non-isothermal effects due to reaction and the heat transfer with the oven. Their model includes two steps for NOx storage: one for fast and one for slow NOx adsorption. Experimentally and computationally, they showed that only a fraction of the total barium is used for NOx storage. In terms of modeling Di-Air or the RPR process, Ting et al. created a 'fast cycling' LNT model with H<sub>2</sub> as the reductant [22]. In order to associate their model with experimental data, it was necessary to include axial mixing of the feed gas as well as the residence time inside the FTIR gas analyzer cell. The lean/rich pulses cannot simply be modeled as a stepwise change. During the mixed lean/rich period the efficiency of NH<sub>3</sub> oxidation from oxygen stored on ceria increased. NH<sub>3</sub> adsorption on the support also increased. This led to a decrease in NH<sub>3</sub> selectivity. Non-isothermal temperature effects were also included. Traditionally, LNT models are built using mid-bed temperature measurements. They found that while the mid-bed temperatures are relatively constant, the front face temperature can be up to 250 °C higher. Their model predicts fast cycling will maintain ~100 °C hotter. NOx slip can occur at the front of the lean phase when temperatures are above 450 °C because of the NOx storage capacity's temperature dependence.

In the current study we have modeled the RPR process by implementing a global kinetic model with propylene as the main reductant, without inclusion of any special reaction or surface intermediates proposed other than those used for conventional LNTs. The model parameters were tuned to fit a large set of low frequency lean/rich switching experiments in the range of 300–600 °C feed gas temperatures which successfully modeled the low frequency behavior of typical LNT process. The same model parameters were employed using high-frequency measurements of boundary conditions to model the moderate-to-high frequency behavior of the RPR process. The model results provide insight into the mechanisms of the frequency dependence of NOx conversion in different operating regimes. In addition, this model was used to explore the washcoat mass transfer limitations on the RPR process which was observed in experiments.

## 2. Global kinetic model

Here the 23-step global kinetic model employed for the RPR process is based on previously suggested models for conventional LNTs with

NOx and oxygen storage capacity, using propylene as the reducing agent such as Refs. [15,16]. Table 1 lists the reactions, corresponding active sites. The rate expressions are listed in Table 2, where the square brackets indicate the molar concentration of each species. The corresponding rate parameters and inhibition functions (or other functions used in rate expressions) are included in Tables S3 and S4 of the Supporting information. In this model, either a power law or a Langmuir–Hinshelwood (LH) structured rate expression is employed. A power law expression, which works well over small ranges, was used for some of the reactions, including the reversible reactions used in this model [23]. The LH rate expression accounts for the inhibition effects due to adsorbed species that are covering the surface sites on the catalyst without the need for including additional inhibition factors. It is important to capture the effect of inhibition in LNTs, for instance, the inhibition of NOx storage by CO<sub>2</sub> is well known and is considered automatically in the LH rate expression [17].

For the NO oxidation, reaction (RXN) 5, a reversible power law model based on thermodynamic equilibrium constant is employed. A reversible reaction is required here for NO oxidation, since a considerable concentration of NO<sub>2</sub> occurs in the feed gas in some of the experiments that drives the reaction in the reverse direction at temperatures of interest in this study. A similar reversible power law form is considered for the water gas shift (WGS), RXN 6, which is also required here due to the high rate of reverse WGS at high temperatures during the RPR process. For the rest of the reactions, a non-reversible rate expression is employed.

A temperature-dependent equilibrium total barium coverage was used for the NOx storage and reduction reactions. At each temperature, the equilibrium total barium coverage, function G<sub>5</sub> in Table S3 of Supporting information, is multiplied by the number of NOx storage sites in the model. This has two effects, first it directly scales the available NOx storage at each temperature, and second it changes the rate of NOx storage/reduction as they scale with number of sites. This equilibrium barium coverage is based on the apparent NOx storage capacity, shown in Fig. 1, which was measured under lean/rich switching conditions as a function of temperature for the LNT sample with the procedure described in S.1 of the Supporting information. As can be seen, the NOx storage curve can be deconvoluted into two Gaussian peaks, low temperature and high temperature, which can be attributed to nitrite and nitrate storage surface species [24]. However, in this model no distinction was made between these two species and only the collective NOx storage capacity was employed. The numerical value of the equilibrium total barium coverage can be found in Table S3 (function G5) of the Supporting information. Four reducing agents are included in this model (H<sub>2</sub>, NH<sub>3</sub>, CO, and C<sub>3</sub>H<sub>6</sub>), which can reduce the stored NOx on barium nitrate as well as gas phase NO, NO<sub>2</sub>, and O<sub>2</sub>. Although the catalyst used in this study did not contain ceria, the surface oxygen storage can be modeled as ceria, RXN 19, which can also be reduced by the aforementioned reductants.

## 2.1. Governing equations

A 2D quasi-steady flow field in the gas phase is assumed which is obtained by solving an incompressible Navier-Stokes momentum equation (Eq. (1)) along the channels of the monolith [25]. This includes the pressure drop in channels, and variations in fluid properties as a function of local temperature. A quasi-steady, pseudo-3D (2D + 1) scalar transport model for mass transport in gas phase and mass transport + reaction in the solid phase is employed which accounts for axial mixing of species due to advection and diffusion in monolith channels. In Eq. (2),  $D$  is the diffusivity in gas or solid phase as will be discussed in Section 6, the term in the left hand side is the advection term which is only included in gas phase, and  $S_i$  is the source term due to reaction which is only included for the solid phase [26].

$$\frac{\partial u}{\partial x} = -\frac{1}{\rho} \frac{\partial p}{\partial x} + \nu \left( \frac{\partial^2 u}{\partial x^2} + \frac{\partial^2 u}{\partial x^2} \right) \quad (1)$$

$$\nabla \cdot (\rho \vec{u} c_i) = \nabla \cdot (D_i \nabla c_i) + S_i \quad (2)$$

The energy equation in gas and solid phase are shown in Eqs. (3) and (4) respectively. In both equations it has been assumed that the lateral temperature variation across the channel and across the thickness of the washcoat is negligible compared to axial temperature gradients along the channel [27]. In Eq. (4) the monolith is considered adiabatic with no heat transfer to the environment, i.e.,  $h_{amb} = 0$ , this closely resembles the experimental condition where the monolith was placed at the edge of the oven which was not exposed to radiative heat transfer. The numerical values of parameters in Eqs. (3) and (4) are listed in the Section S.3.2 of the Supporting information.

$$u_m \rho_g C_{p,g} \frac{\partial T_g}{\partial x} + h \cdot G_A \cdot (T_g - T_s) = 0 \quad (3)$$

$$\rho_s \cdot C_{p,s} \cdot \frac{\partial T_s}{\partial t} = k_s \cdot \frac{\partial^2 T_s}{\partial x^2} + h \cdot G_A \cdot (T_g - T_s) - h_{amb} \cdot S_{ext} \cdot (T_s - T_{amb}) + \sum_{i=1}^m (-\Delta H)_i \cdot R_i \quad (4)$$

## 2.2. Pulse mixing and product mixing

Two types of mixing can be considered in the model, in addition to the kinetics model of the monolith, as shown schematically in Fig. 2. First is the reductant pulse mixing upstream of the monolith, which changes the concentration profile at the catalyst inlet from a rectangular pulse, to a smeared pulse as shown in the left part of Fig. 2. This is referred to as “pulse mixing” in the rest of this study. We will discuss in Section 5, how the “pulse mixing” was included in the model.

The second is the “product mixing”, which accounts for axial mixing of catalyst effluent in the lines connecting the reactor to the measurement instruments plus the mixing and attenuation in the gas chamber of the gas analysis instrument (FTIR). This is modeled effectively by applying a first order low pass filter to the catalyst outlet concentration time series, with the transfer function shown in Eq. (5). In this equation,

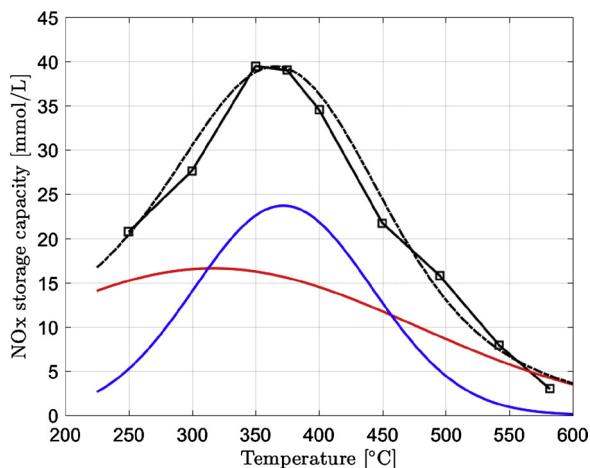
**Table 1**  
Global kinetic model for lean NOx trap with propylene as the reducing agent.

#	Reaction type	Reaction step	site
1	Oxidation	CO + 0.5 O <sub>2</sub> ⇒ CO <sub>2</sub>	PGM
2		H <sub>2</sub> + 0.5 O <sub>2</sub> ⇒ H <sub>2</sub> O	PGM
3		C <sub>3</sub> H <sub>6</sub> + 4.5 O <sub>2</sub> ⇒ 3 CO <sub>2</sub> + 3 H <sub>2</sub> O	PGM
4		2NH <sub>3</sub> + 1.5 O <sub>2</sub> ⇒ N <sub>2</sub> + 3 H <sub>2</sub> O	PGM
5		NO + 0.5 O <sub>2</sub> ⇌ NO <sub>2</sub>	PGM
6	WGS and reforming	H <sub>2</sub> O + CO ⇌ CO <sub>2</sub> + H <sub>2</sub>	PGM
7		C <sub>3</sub> H <sub>6</sub> + 3 H <sub>2</sub> O ⇒ 3 CO + 6 H <sub>2</sub>	PGM
8		CO + NO ⇒ CO <sub>2</sub> + 0.5 N <sub>2</sub>	PGM
9	NOx reduction	C <sub>3</sub> H <sub>6</sub> + 9 NO ⇒ 3 H <sub>2</sub> O + 3 CO <sub>2</sub> + 4.5 N <sub>2</sub>	PGM
10		C <sub>3</sub> H <sub>6</sub> + 9 NO <sub>2</sub> ⇒ 3 H <sub>2</sub> O + 3 CO <sub>2</sub> + 9 NO	PGM
11		2 NH <sub>3</sub> + 3 NO ⇒ 2.5 N <sub>2</sub> + 3 H <sub>2</sub> O	PGM
12	NOx storage	BaCO <sub>3</sub> + 2 NO <sub>2</sub> + 0.5 O <sub>2</sub> ⇒ Ba(NO <sub>3</sub> ) <sub>2</sub> + CO <sub>2</sub>	Barium
13		BaCO <sub>3</sub> + 2 NO + 1.5 O <sub>2</sub> ⇒ Ba(NO <sub>3</sub> ) <sub>2</sub> + CO <sub>2</sub>	Barium
14		Ba(NO <sub>3</sub> ) <sub>2</sub> + 3 CO ⇒ BaCO <sub>3</sub> + 2 CO <sub>2</sub> + 2 NO	Barium
15	NOx reduction	Ba(NO <sub>3</sub> ) <sub>2</sub> + 3 H <sub>2</sub> + CO <sub>2</sub> ⇒ BaCO <sub>3</sub> + 3 H <sub>2</sub> O + 2 NO	Barium
16		Ba(NO <sub>3</sub> ) <sub>2</sub> + 1/3 C <sub>3</sub> H <sub>6</sub> ⇒ BaCO <sub>3</sub> + H <sub>2</sub> O + 2 NO	Barium
17		Ba(NO <sub>3</sub> ) <sub>2</sub> + 10/3 NH <sub>3</sub> + CO <sub>2</sub> ⇒ BaCO <sub>3</sub> + 5 H <sub>2</sub> O + 8/3 N <sub>2</sub>	Barium
18	Ammonia formation	8H <sub>2</sub> + Ba(NO <sub>3</sub> ) <sub>2</sub> + CO <sub>2</sub> ⇒ 2NH <sub>3</sub> + BaCO <sub>3</sub> + 5H <sub>2</sub> O	Barium
19		2.5 H <sub>2</sub> + NO ⇒ NH <sub>3</sub> + H <sub>2</sub> O	PGM
20		PGM + 0.5 O <sub>2</sub> ⇒ PGM-O	PGM-OSC
21	Oxygen storage and reduction	PGMO + CO ⇒ PGM + CO <sub>2</sub>	PGM-OSC
22		PGMO + H <sub>2</sub> ⇒ PGM + H <sub>2</sub> O	PGM-OSC
23		PGMO + 1/9 C <sub>3</sub> H <sub>6</sub> ⇒ PGM + 1/3 CO <sub>2</sub> + 1/3 H <sub>2</sub> O	PGM-OSC

**Table 2**

Rate expressions corresponding to reactions listed in Table 1.

	Rate function
1	$\frac{k_1 [CO] G_4}{G_1 G_2 G_3}$
2	$\frac{k_2 [H_2] [O_2]^{1.6}}{G_1 G_2 G_3}$
3	$\frac{k_3 K_{C_3H_6,ads}^{eq} K_{O_2,ads}^{eq} [C_3H_6] [O_2]}{(1 + K_{C_3H_6,ads}^{eq} [C_3H_6] + K_{O_2,ads}^{eq} [O_2] + K_{CO_2,des}^{eq} [CO_2] + K_{H_2O,des}^{eq} [H_2O])^2}$
4	$k_4 [NH_3] [O_2]$
5	$k_5 \left[ \{NO\} [O_2]^{1/2} - \frac{[NO_2]}{K_5^{eq}} \right]$
6	$k_6 \left[ \{H_2O\} [CO] - \frac{\{CO_2\} [H_2]}{K_6^{eq}} \right]$
7	$k_7 [C_3H_6] [H_2O]$
8	$k_8 [CO] [NO]$
9	$\frac{k_9 K_{NO,ads}^{eq} K_{C_3H_6,ads}^{eq} [NO] [C_3H_6]}{(1 + K_{NO,ads}^{eq} [NO] + K_{C_3H_6,ads}^{eq} [C_3H_6] + K_{CO_2,des}^{eq} [CO_2] + K_{H_2O,des}^{eq} [H_2O])^2}$
10	$k_{10} [NO_2] [C_3H_6]$
11	$k_{11} [NH_3] [NO]$
12	$\frac{k_{12} K_{NO_2,ads}^{eq} K_{O_2,ads}^{eq} [NO_2] [O_2] (\theta_{BaCO_3} G_5)}{(1 + K_{NO_2,ads}^{eq} [NO_2] + K_{O_2,ads}^{eq} [O_2] + K_{CO_2,des}^{eq} [CO_2])^2}$
13	$\frac{k_{13} K_{NO,ads}^{eq} K_{O_2,ads}^{eq} [NO] [O_2] (\theta_{BaCO_3} G_5)}{(1 + K_{NO,ads}^{eq} [NO] + K_{O_2,ads}^{eq} [O_2] + K_{CO_2,des}^{eq} [CO_2])^2}$
14	$k_{14} [CO] (\theta_{Ba(NO_3)_2} G_5)$
15	$k_{15} [H_2] (\theta_{Ba(NO_3)_2} G_5)$
16	$\frac{k_{16} K_{C_3H_6,ads}^{eq} [C_3H_6] (\theta_{Ba(NO_3)_2} G_5)}{1 + K_{C_3H_6,ads}^{eq} [C_3H_6] + K_{H_2O,des}^{eq} [H_2O] + K_{NO,des}^{eq} [NO]}$
17	$k_{17} [NH_3] [CO_2] (\theta_{Ba(NO_3)_2} G_5)$
18	$r_{18} = k_{18} [H_2] [CO_2] (\theta_{Ba(NO_3)_2} G_5)$
19	$k_{19} [H_2]^2 [NO]^{0.25}$
20	$k_{20} [O_2] \theta_{PGM}$
21	$k_{21} [CO] \theta_{PGMO}$
22	$k_{22} [H_2] \theta_{PGMO}$
23	$k_{23} [C_3H_6] \theta_{PGM}$

**Fig. 1.** Apparent NOx storage capacity of LNT sample (details in Supporting information section S.1). The dashed line shows the fitted curve which can be deconvoluted into low temperature and high temperature Gaussian peaks.

$s$  is the Laplace parameter, and the time constant  $\tau_{mix} = 1.7$  s is obtained by measuring the rise time of the concentration signal obtained from the FTIR as the response of the entire reactor plus gas analysis instrument to a step input in concentration at a constant total flow rate.

$$\frac{C_{out}}{C_{in}}(s) = \frac{1}{1 + \tau_{mix}s} \quad (5)$$

### 3. Low-frequency experiments for model fitting

Tests were run with a research Pt–Rh/Ba/Al<sub>2</sub>O<sub>3</sub> LNT monolith with 3.18 g/L of precious metal with the ratio of Pt/Pd/Rh = 8/0/1. The washcoat contained barium, a proprietary high temperature NOx storage component and no ceria. The sample contains a small amount (400 mg/L) of oxygen storage capacity (OSC), which is attributed to the PGM sites and are labeled as PGM-OSC sites in this mechanism. The kinetic parameters were tuned to fit the low frequency response of the LNT. For this purpose, a series of long duration lean/rich/lean switches were used. The data was taken from a differential reactor (at space velocity of 150,000 h<sup>−1</sup>) by varying feed temperature and concentrations of NO, NO<sub>2</sub>, CO<sub>2</sub>, O<sub>2</sub>, and propylene, as indicated in Table 3, balanced in Ar to enable detection of N<sub>2</sub> formation. The experiments were done at inlet gas temperatures of 300, 450, and 600 °C. A partial factorial design of experiment with three levels of species concentration was employed which led to 28 experiments at each temperature level, a total of 84 experiments. A detailed description of the experimental setup of the reactor as well as the rapid pulsing system can be found in Ref. [4].

Due to non-linear LH rate expressions, it was not possible to obtain the rate parameters using linear regression; therefore, multivariable nonlinear optimization was employed to minimize the error of the model results with respect to lean/rich switching experiments. The objective function (to be minimized) was the L2 norm of the difference between the time-series indicating the model and experimental values of the output concentration for a large range of switching experiments. This was summed over all species considered in the model to obtain the total value of objective function. In order to avoid biasing the model to species with large absolute concentrations, such as CO<sub>2</sub> and H<sub>2</sub>O with 5–10% molar concentration, all the concentration values were first z-score scaled [28]. A genetic algorithm, MATLAB's GA toolbox, was implemented with constraints on physical values of rate parameters. An initial guess for the optimization was obtained using the rate parameters available in the literature.

Fig. 3 schematically shows a lean/rich/lean switch test. Prior to each switch test, the catalyst surface was pre-treated at the experiment temperature by saturation of the surface oxygen and NOx storage with 5% O<sub>2</sub> and 1000 ppm NOx levels corresponding to the experimental lean flow concentration (listed in Table 3) for 10 min. Therefore, for the model tuning purpose it was assumed that after the pretreatment at the start of the experiment the surface coverages are  $\theta_{Ba(NO_3)_2} = 1$ , and  $\theta_{Ce_2O_4} = 1$ . The experiment was started with 15 s of lean flow containing CO<sub>2</sub>, O<sub>2</sub>, and NOx, followed by 60 s of rich flow containing CO<sub>2</sub>, NOx, and C<sub>3</sub>H<sub>6</sub>, followed by 180 s of lean flow.

#### 3.1. Discussion of lean/rich switching experimental results

In this section we discuss the general trends observed in the large set of switching experiments and the conclusions that can be derived from these observations towards the kinetic model fitting process. As an example, Fig. 4 shows the results of a single switching experiment with the inlet composition of 800 ppm NO<sub>2</sub>, 5% O<sub>2</sub> during lean periods and 800 ppm NO<sub>2</sub>, 1000 ppm C<sub>3</sub>H<sub>6</sub> during the rich pulse. The catalyst bed temperature, Fig. 4(a), shows an initial large peak with a temperature increase of 31 °C in the case of  $T_{inlet} = 300$  °C, and a temperature increase of 55 °C for both  $T_{inlet} = 450$  °C and  $T_{inlet} = 600$  °C, at the lean/rich switch. In addition, smaller peaks with temperature increases of 8 °C and 21 °C are observed for  $T_{inlet} = 450$  °C and  $T_{inlet} = 600$  °C, respectively, at the rich/lean switch. This entire experimental temperature trace was then used as a direct input to the model during the tuning process to extract the rate parameters.

To explain these peaks, since there is no oxygen during the rich pulse, the first temperature peak is attributed to the exothermic reduction of stored surface NOx and oxygen, which diminishes by depletion of these surface species as the rich period is continued. It should



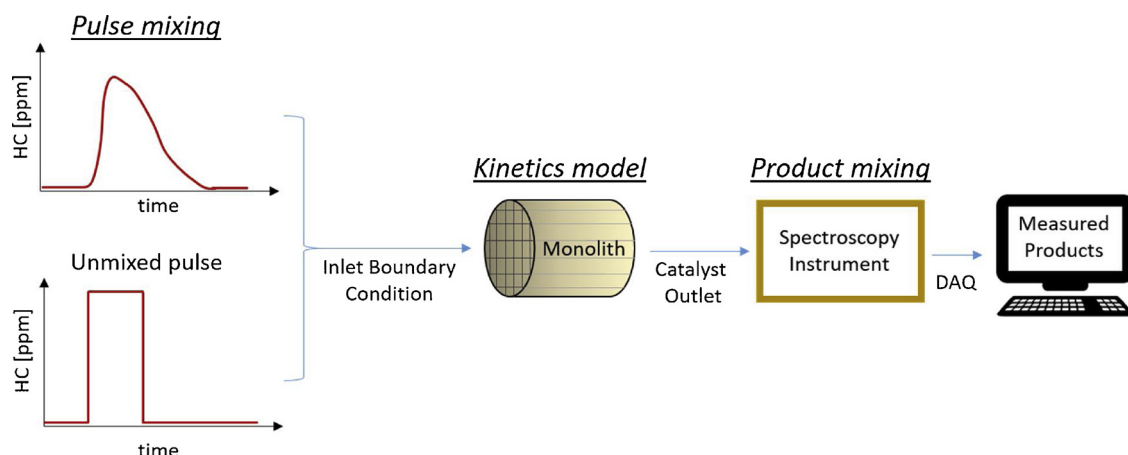


Fig. 2. Schematics of pulse mixing, kinetics model, and product mixing model considered for modeling the RPR reaction.

Table 3

List of concentrations and temperatures in low frequency switching experiments used for obtaining rate parameters of the model.

Levels	Test Variables					
	Temperature [°C]	NO [ppm]	NO <sub>2</sub> [ppm]	CO <sub>2</sub> [%]	O <sub>2</sub> [%]	C <sub>3</sub> H <sub>6</sub> (rich pulse) [%]
Low	300	0	0	0	0.2	0.1
Medium	450	200	200	1	1	0.5
High	600	800	800	10	5	2

be mentioned that, for a short period of time after switching from lean to rich flow, there is some remaining gas phase O<sub>2</sub> available due to gas phase mixing which also contributes to the first exothermic peak. The second peak can be attributed to two possible sources; (a) co-existence of oxygen and propylene in the gas phase feed for a short period of time (on the order of ~1 s) after the rich/lean switch due to axial mixing of the rich and lean feeds and/or (b) the presence of surface hydrocarbon intermediates which are exothermically oxidized after the rich/lean switch.

Fig. 4(b)–(i) show the measured concentrations of the main reaction products, i.e., O<sub>2</sub>, C<sub>3</sub>H<sub>6</sub>, NO<sub>x</sub>, CO<sub>2</sub>, CO, H<sub>2</sub>O, NH<sub>3</sub>, and H<sub>2</sub>. As can be seen in Fig. 4(c), a few seconds after the lean/rich switch C<sub>3</sub>H<sub>6</sub> shows a small breakthrough peak, followed by a dip in concentration and a final steady state breakthrough. The C<sub>3</sub>H<sub>6</sub> breakthrough has a clear negative correlation with catalyst bed temperature, i.e., the dip in breakthrough occurs at the same time that the peak in temperature occurs tracking the increased rate of C<sub>3</sub>H<sub>6</sub> consumption (oxidation, partial oxidation, or decomposition) as the bed temperature is increased. The steady C<sub>3</sub>H<sub>6</sub> deficit at the end of the rich pulse is due to kinetically rate-limited oxidation for a T<sub>inlet</sub> = 300 °C, and is limited by stoichiometry by the amount of available oxygen from feed NO at T<sub>inlet</sub> = 450 °C, and T<sub>inlet</sub> = 600 °C. Therefore, it can be safely assumed that the oxygen and NO<sub>x</sub> storage sites have been almost fully depleted at the end of the rich pulse, i.e.,  $\theta_{Ba(NO_3)_2} = 0$  and  $\theta_{Ce_2O_4} = 0$  as shown in Fig. 3. These values

of the surface coverages at the beginning of the rich pulse and lean pulse have been used as initial conditions for the fitting of kinetic parameters.

Two peaks are observed in the ammonia concentration of Fig. 4(h) where there is a sharper first peak and a broader second peak. Fig. 5 shows similar behavior for various concentrations of C<sub>3</sub>H<sub>6</sub> and NO at the inlet for T<sub>inlet</sub> = 450 °C. By comparing the red and black curves in Fig. 5, it can be seen that the first peak of ammonia increases with an order smaller than 1/2 due to an increase in the C<sub>3</sub>H<sub>6</sub> level. Conversely, the first peak has almost no dependence on the inlet NO level; this, in conjunction with the short duration of the peak, suggests a reaction of H<sub>2</sub> with the stored surface NO<sub>x</sub>, which is modeled by RXN 18. The second peak which exhibits an almost first order (order of 1.18 in this case) dependence on NO level, which can be modeled using RXN 19, comes from the direct reduction of the NO with H<sub>2</sub>. It is noteworthy that H<sub>2</sub> was not fed to the reactor, and the sources of H<sub>2</sub> formation are steam reforming and water gas shift that are included in the kinetic model (Table 1).

#### 4. Fitted model performance evaluation

To show the goodness of the fitted model, Fig. 6 shows predictions of the model for the lean/rich switching experiments with an inlet composition of 800 ppm NO, 5% O<sub>2</sub> during lean periods and 800 ppm

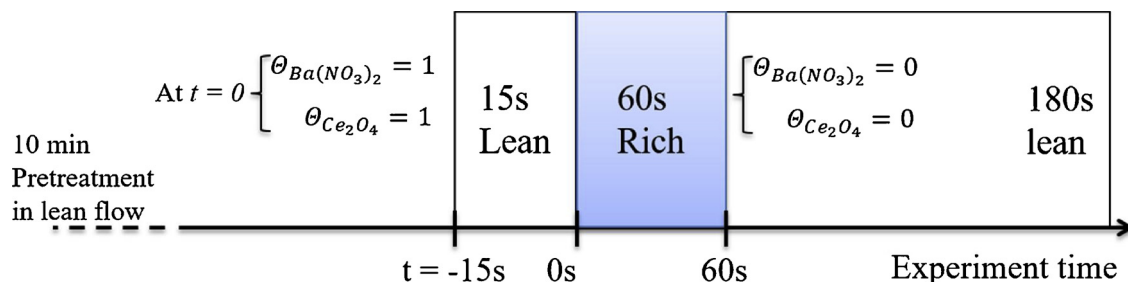


Fig. 3. Schematics of lean/rich/lean switch showing lean flow pretreatment followed by a rich/lean pulse.

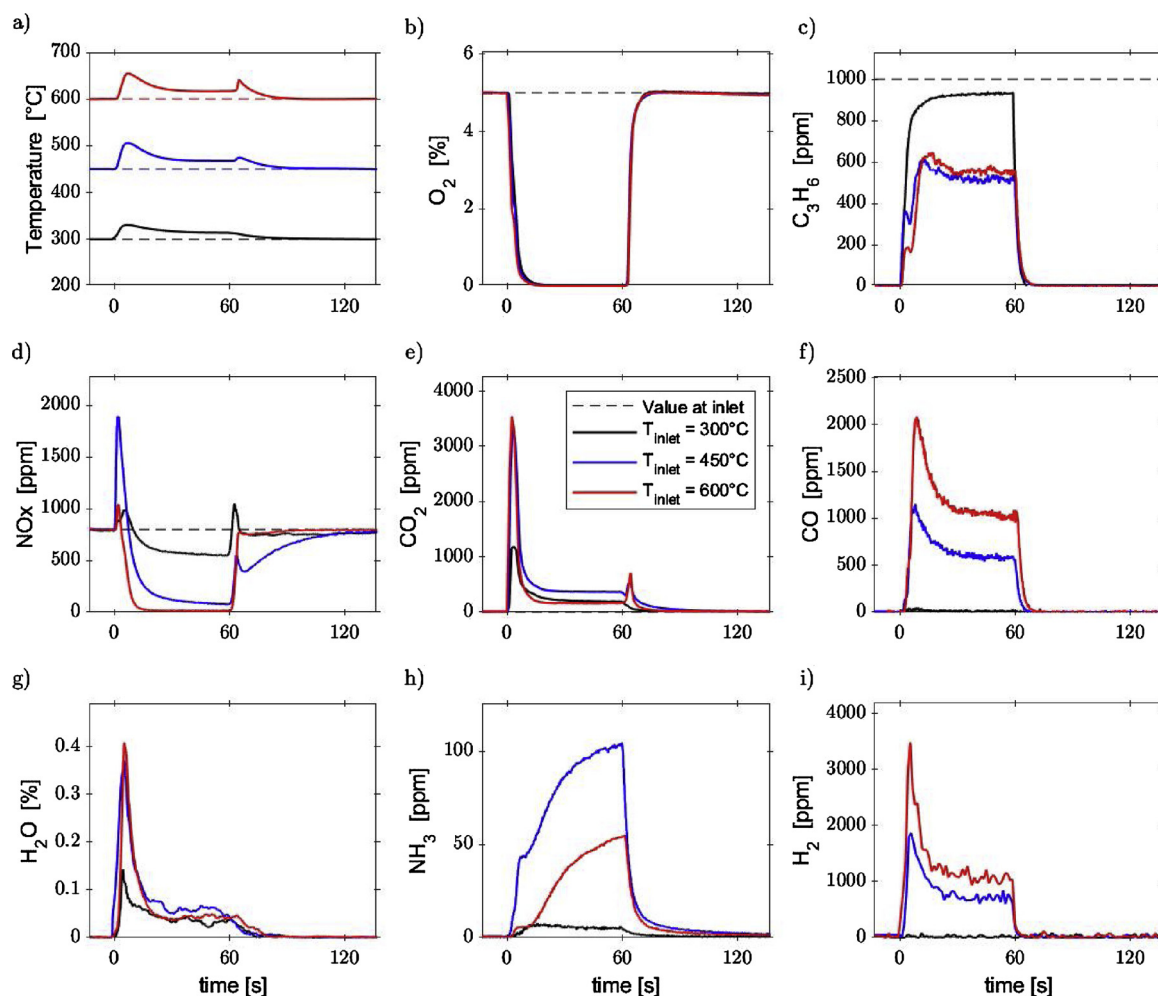


Fig. 4. A sample result of pulsing experiments from a differential reactor, at  $SV = 150,000 \text{ h}^{-1}$  with inlet concentrations of 800 ppm  $\text{NO}_2$ , 1%  $\text{O}_2$  during lean periods and 800 ppm  $\text{NO}_2$ , 1000 ppm  $\text{C}_3\text{H}_6$  during the rich pulse. The pulse start and end times ( $t = 0$ , and  $t = 60 \text{ s}$  respectively) are shown on the x-axis of each plot. Line colors correspond to different inlet temperatures, legend shown in part (e).

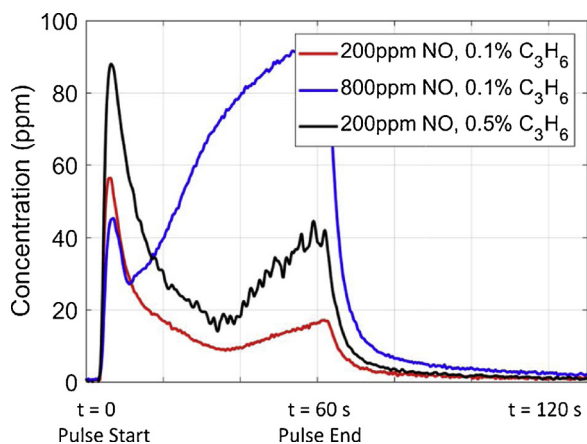


Fig. 5. Ammonia concentration during a rich pulse at different feed gas compositions, at  $450^\circ\text{C}$  inlet temperature, showing the trends of first and second peaks as the concentration of NO and propylene are varied.

$\text{NO}$ , 1000 ppm  $\text{C}_3\text{H}_6$  during the rich pulse at  $T_{\text{inlet}} = 450^\circ\text{C}$ . It can be seen that, including the product mixing model is necessary to obtain good agreement with the experiments both in terms of signal phasing (due to transport delays) and smoothness of species traces during switching transients. The fitted model is in good agreement with the experimental switching results in a wide range of operating conditions

and is capable of reproducing the main features of the reaction products. However, there are some discrepancies observed between the model results and a specific set of experimental data, such as not resolving the  $\text{NO}_x$  puff in some cases (for example in Fig. 6(b)). This is due to the use of a single optimization process (and therefore, a single set of rate parameters) over a large range of inlet concentrations, where minimizing the RMS error in this entire range does not necessarily minimize the error for a single inlet concentration.

## 5. Model predictions at high pulsing frequencies

The kinetic rate parameters obtained from fitting the model to switching experiments were exactly used to study the low (corresponding to traditional LNT switching) to high frequency regimes of the RPR process (1/60–5 Hz). Therefore, the main purpose of this study is to understand whether the low frequency mechanistic models for typical LNTs are accurate for high frequency RPR operation. Two definitions of the inlet boundary conditions were used in the model (where the reductant pulses are delivered to the catalyst). In the first choice (kinetics only model) the reductant concentration was changed from a lean to a rich condition using a sharp step function independent of pulsing frequency and temperature, as shown with dashed red lines in Fig. 7. In the second choice (kinetics + pulse mixing model) the direct measurement of the reductant concentration (propylene in this case) at the inlet of the catalyst was used based on high-speed FID measurements (at 200 Hz sampling rate). The solid black line in Fig. 7 shows

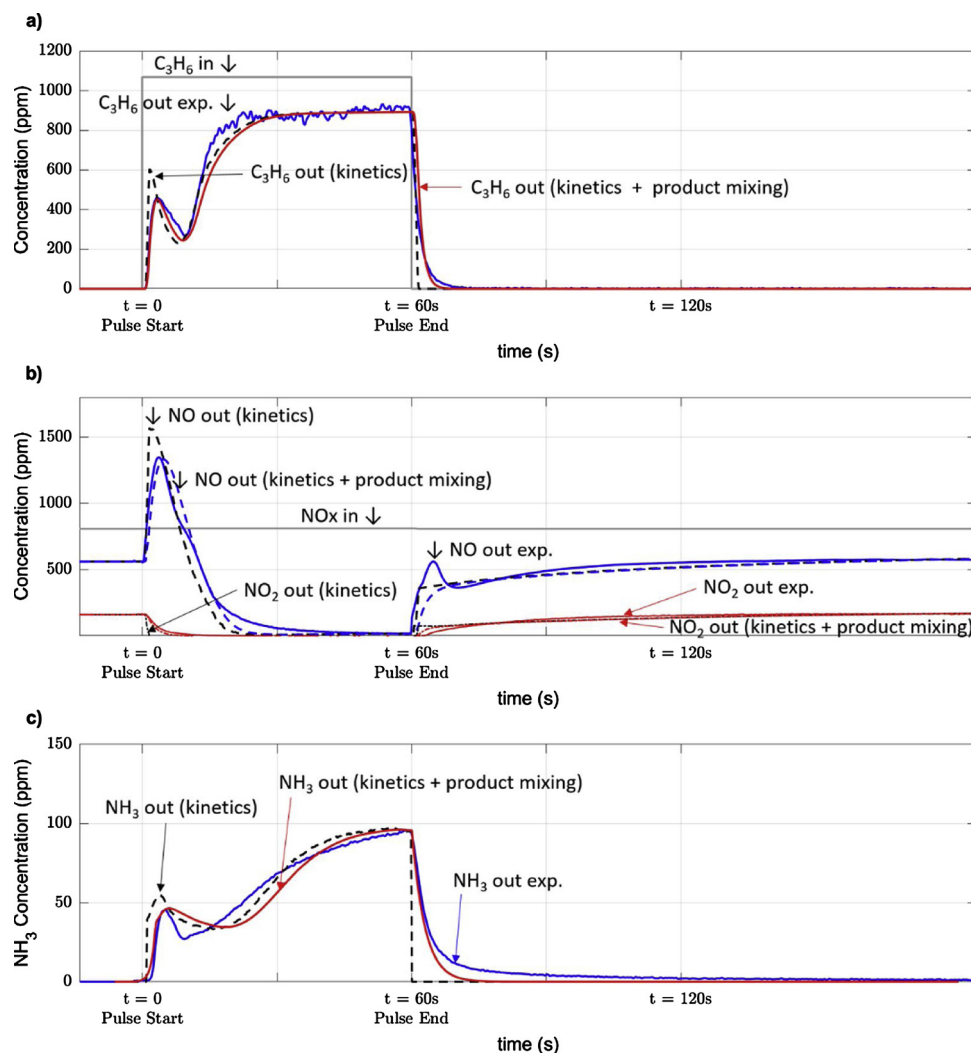


**Fig. 6.** Fitted model results for switching experiments with 800 ppm NO, 5% O<sub>2</sub> during lean periods and 800 ppm NO, 1000 ppm C<sub>3</sub>H<sub>6</sub> during the rich pulse at 450 °C inlet temperature, showing, a) C<sub>3</sub>H<sub>6</sub>, b) NO and NO<sub>2</sub>, and c) NH<sub>3</sub> concentrations. Blue solid lines show experimental data, dashed lines show the “kinetics” model results, while red solid lines show results of the kinetics model including product mixing. (For interpretation of the references to colour in this figure legend, the reader is referred to the web version of this article).

high-speed HC measurements at the inlet of the catalyst at 300 °C and 600 °C and a number of pulsing frequencies. These reductant pulses have been generated using a specifically designed mixer discussed elsewhere [14]. It can be seen that the effect of pulse mixing in the leading and trailing edges of the pulse significantly increases by increasing the pulsing frequency (note the differing x-axis scales in Fig. 7). In addition, the pulse mixing increases at high temperatures which is due to increased molecular diffusivity of the gas, as well as increased mean volumetric flow velocity at higher temperatures which promotes advective mass transfer. Here we can define the rich fraction of the HC pulses as the ratio of the amount of the HC which results in a rich mixture at the inlet of the monolith to the total amount of HC injected in a pulse (see Eq. (6)). Fig. 8 shows the rich fraction of HC pulses as a function of pulsing frequency and inlet flow temperature (holding commanded pulse duty cycle constant), which indicates significant reduction in rich fraction of the pulse as the pulsing frequency and temperature are increased. As we will discuss later, these observations on reductant pulse mixing have profound impacts on the high frequency results of the model.

$$f_r = \frac{\int_{t: \lambda(t) < 1} c_{HC}(t) dt}{\int c_{HC}(t) dt} \quad (6)$$

Fig. 9(a) illustrates the cycle-averaged NOx conversion over a large range of pulsing frequencies from typical LNT operation (0.01 Hz) to a high-frequency RPR regime (> 1 Hz) with the feed gas concentration shown in Table 4 for a 30,000 h<sup>-1</sup> space velocity at 600 °C. As can be seen, there is an optimal frequency of order 0.3–1 Hz, which maximizes the NOx conversion at a constant fuel penalty associated with HC pulses at any feed gas temperature. The global kinetic model is able to predict the improvements in NOx conversion as the pulsing frequency is increased. As will be further discussed (in Fig. 12), this improvement can be mainly attributed to shorter NOx storage periods and improvement in the NOx storage efficiency which is captured with the model. However, the kinetic model alone does not predict the decline in NOx conversion as the frequency is further increased. The axial mixing and attenuation of reductant pulses, which is considered to be the primary mechanism of the decrease in NOx conversion at higher frequencies, must be included in the model to predict the reduction in NOx conversion at high frequencies and predict the optimal pulsing frequency. The modeling of axial pulse mixing upstream of the monolith requires an unsteady 3D CFD model which is not in the scope of the present work. Therefore, the pulse mixing was empirically measured in the bench reactor using a Combustion Fast FID analyzer (at 200 Hz sampling frequency), as shown in Fig. 7. These results were imposed directly on the model as the inlet gas concentration boundary condition.

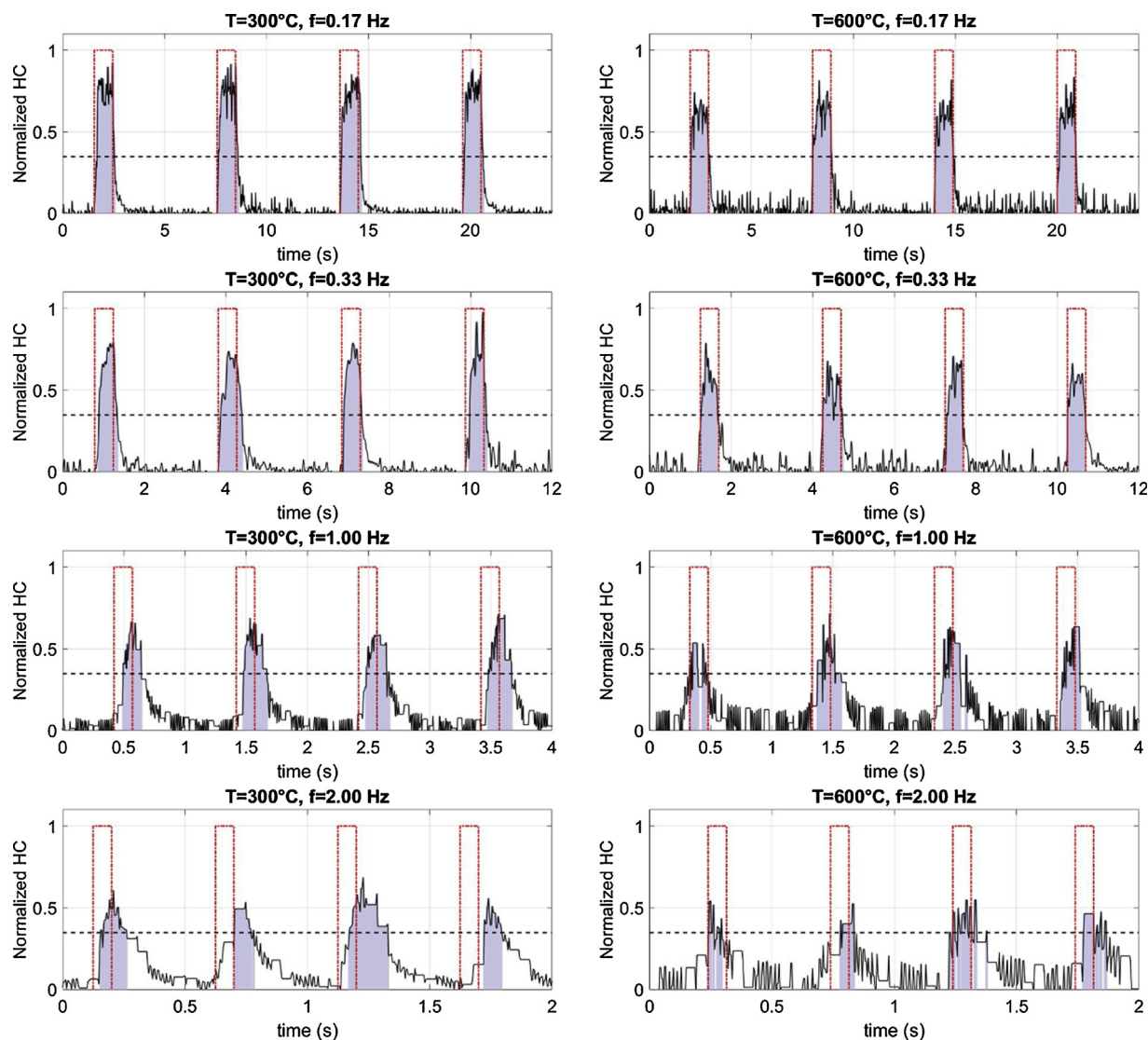


Fig. 7. High speed HC pulse measurements at the inlet of the catalyst at two temperatures of 300 °C and 600 °C and at different pulsing frequencies. The black dashed line shows the stoichiometric level of the HC, and the gray shaded areas show the rich parts of the pulse. The HC pulses are generated using a specifically designed mixer described in Ref. [14].

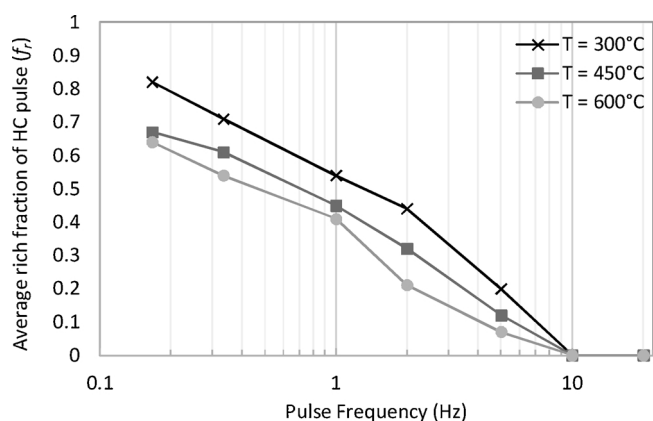
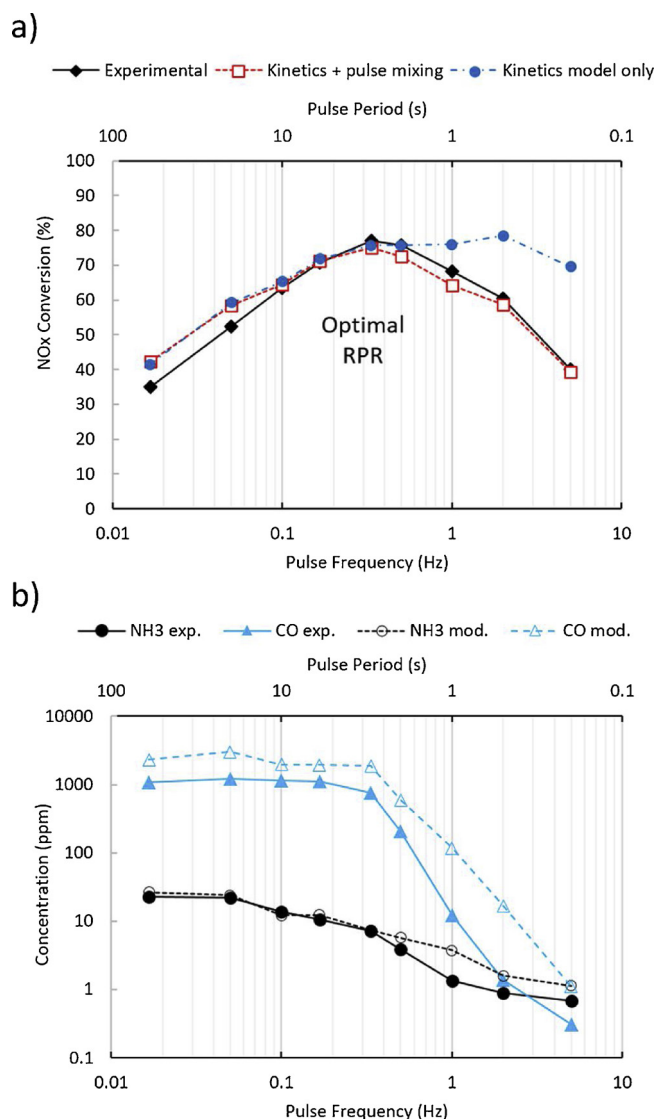


Fig. 8. Average rich fraction of propylene pulse (defined by Eq. 6) at the inlet of the catalyst as a function of pulse frequency and inlet gas temperature.

With the combination of the global kinetic model and the pulse mixing, the agreement with the experimental results in Fig. 9 is excellent and very supportive of using this model to describe the RPR results.

The selectivity of reaction products, CO, NH<sub>3</sub>, and N<sub>2</sub>O is a strong function of temperature and pulsing frequency [29,4,21]. However, since the N<sub>2</sub>O concentration was shown to be very low and not reliably detectable with a ppm-level gas analyzer above 450 °C, which is the temperature range of interest in this study, we have not included N<sub>2</sub>O in the current model. Therefore, here we focus on the concentrations of NH<sub>3</sub> and CO as a function of pulsing frequency which are shown in Fig. 9(b). It can be seen that the “kinetics + pulse mixing” model follows the general trend of the conversion to fall off as the frequency increases above the optimal frequency. However, the model mostly overestimates the concentration of these species which we believe is due to inaccurate capture of surface reaction rate parameters for formation/consumption of these species under high pulsing frequencies. It is noteworthy that, upon further tuning of the model, much better agreement in selectivity of reaction products is achievable; however, this is not the main focus of this study. Previous experimental results indicated that the ammonia concentration peaks in the range of 350–450 °C depending on pulsing frequency [4], and the concentration of ammonia observed at the outlet of the catalyst is very low at 600 °C due to accelerated ammonia oxidation with O<sub>2</sub>, and surface and gas phase NO<sub>x</sub> [30–32]. The decreasing trend of both ammonia and CO as





**Fig. 9.** Model and experimental results at 600 °C inlet temperature, (a) Cycle-averaged NOx conversion showing experimental results as well as the “kinetics” and “kinetics + pulse mixing” model results, (b) cycle-averaged concentration of CO and NH<sub>3</sub> from the “kinetics + pulse mixing” model and experiments as a function of pulsing frequency.

**Table 4**

Feed gas concentration used for experiments and modeling of the RPR process. Concentrations simulate diesel engine exhaust at high loads.

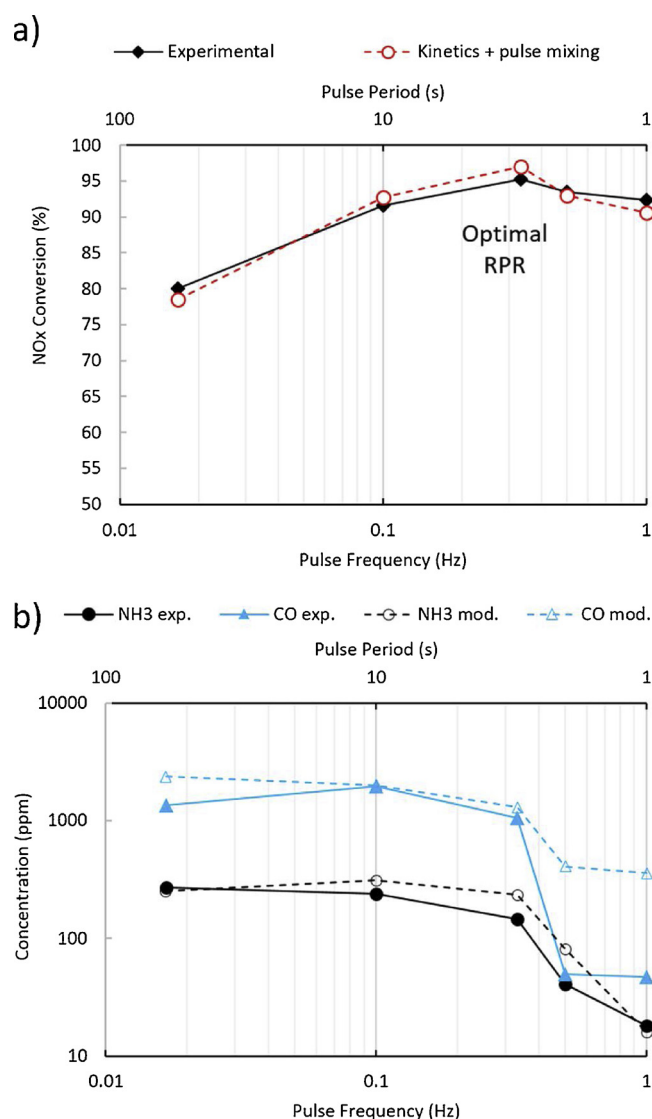
	Lean	Rich (reductant injection)
O <sub>2</sub> (%)	2.87	2.63
CO <sub>2</sub> (%)	11.16	10.25
H <sub>2</sub> O (%)	4.78	4.39
NO (ppm)	676	621
C <sub>3</sub> H <sub>6</sub> (%)	0	1.64
Lambda	1.21	0.76

the pulsing frequency increases at both 450 °C and 600 °C is a result of a) an increased number of pulses per unit time leading to increased oxidation with stored surface oxygen, and b) increased availability of gas phase oxygen due to enhanced pulse mixing at higher frequencies. Fig. 10 shows the experimental and “kinetic + pulse mixing” model results for a temperature of 450 °C, which indicates a less evident peak in NOx conversion vs. frequency, still near 0.3 Hz, which is captured by the model. Similar to the case for 600 °C, a decrease in CO and NH<sub>3</sub>

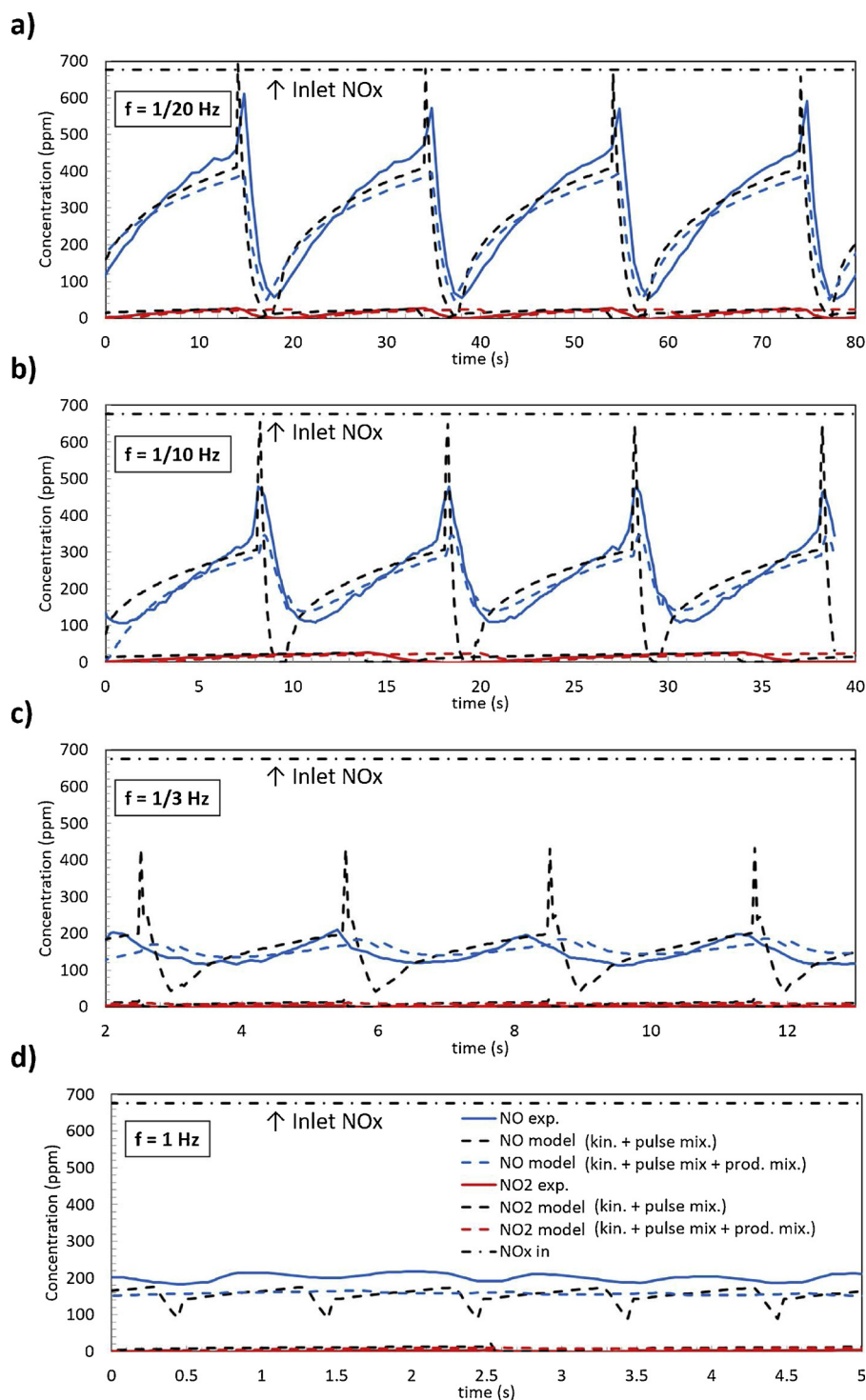
concentrations is observed as the pulsing frequency is increased. However, the NH<sub>3</sub> concentration is much higher at 450 °C compared to 600 °C due to a lower rate of ammonia oxidation.

Fig. 11 illustrates the transient measurements from the bench reactor (at 5 Hz sampling frequency) and corresponding model results. The “kinetics + pulse mixing” model has good agreement with the transient measurements in terms of the mean of the concentrations; however, the amplitude of peaks and dips in the concentrations is significantly overestimated using this model. This issue is solved by including the product mixing downstream of the catalyst in the “kinetics + pulse mixing + product mixing” model, which has good overall agreement with the experimental concentration traces. It should be mentioned that, here the product mixing refers to mixing of the reaction products in the gas lines downstream of the catalyst and in the gas analysis chamber as explained in Section 2.2.

Fig. 12 shows the model results for variations in the surface coverage of the NOx storage sites during the RPR process. It indicates that the amplitude of change in the surface coverage of BaCO<sub>3</sub> and Ba(NO<sub>3</sub>)<sub>2</sub> over each cycle, reduces with increasing pulsing frequency. This means



**Fig. 10.** Model and experimental results at 450 °C inlet temperature, (a) Cycle-averaged NOx conversion showing experimental and “kinetics + pulse mixing” model results, (b) cycle-averaged concentration of CO and NH<sub>3</sub> from the “kinetics + pulse mixing” model and experiments as a function of pulsing frequency.



**Fig. 11.** Transient NO<sub>x</sub> measurements during the RPR process and corresponding model results with feed gas compositions shown in Table 4 with a space velocity of 30,000 h<sup>-1</sup> at 600 °C inlet temperature for pulsing frequencies of (a) 1/20 Hz, (b) 1/10 Hz, (c) 1/3 Hz, (d) 1 Hz.

that the amount of NO<sub>x</sub> storage capacity required to obtain a target NO<sub>x</sub> conversion is reduced by increasing the pulsing frequency. Fig. 12 also lists the average rate of NO<sub>x</sub> storage as is improved at higher frequency, as shown by larger average slope of the Ba(NO<sub>3</sub>)<sub>2</sub> coverage (i.e.  $\alpha$  in Fig. 12) during the storage phase as the pulsing frequency is increased to optimal frequency. The value of  $\alpha$  starts to decrease if the frequency is past the optimal value due to an insufficient prior reduction step caused by attenuation of reductant pulses. At high temperatures this could improve the NO<sub>x</sub> conversion since the storage capacity is limited for lower frequency pulsing (see Fig. 1).

## 6. Mass transfer limitations

The washcoat and external gas phase mass transfer can become significant limiting factors in the mid and high temperature regimes of a monolithic reactor [33]. Since we focus on the high temperature performance of the RPR process, the effect of washcoat mass transfer on RPR performance was studied in a controlled experiment with two monolithic samples of different washcoat thickness. Both of the samples had the same PGM loading of 110 gpcf; however, the average washcoat thickness (containing Ba/Al<sub>2</sub>O<sub>3</sub>) was 40  $\mu$ m for sample  $\alpha$  and 90  $\mu$ m for

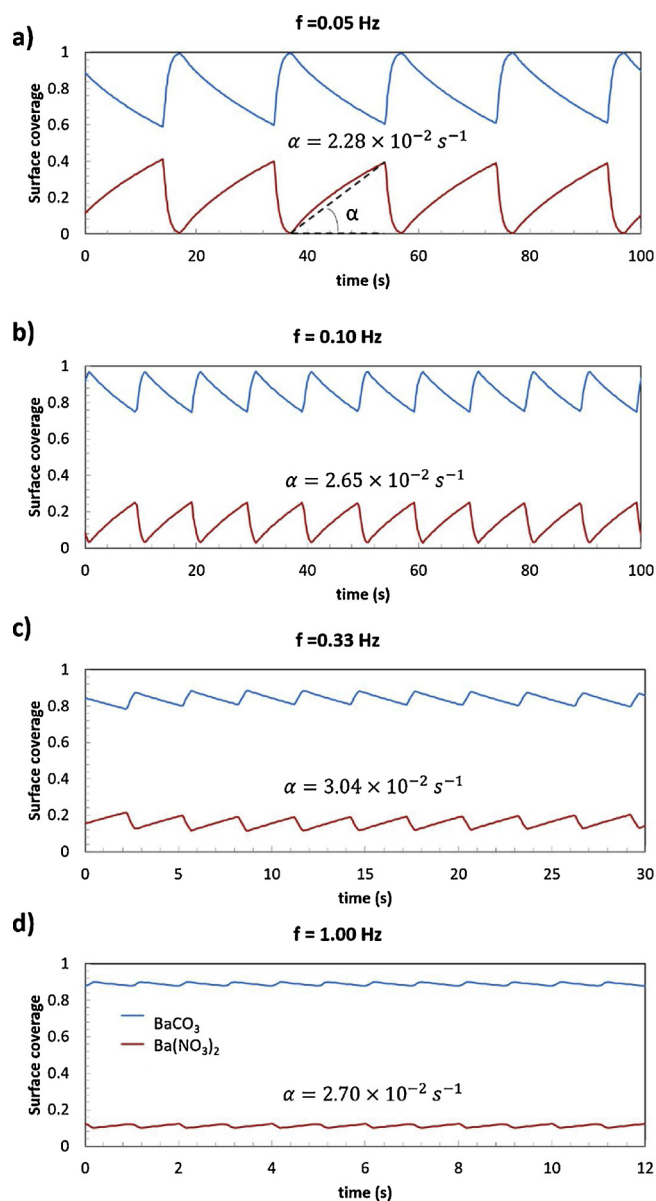


**Fig. 12.** Model results of the variation in surface coverage of  $\text{BaCO}_3$  and  $\text{Ba}(\text{NO}_3)_2$  with feed gas composition shown in Table 4 with a space velocity of  $30,000 \text{ h}^{-1}$  at  $600^\circ\text{C}$  inlet temperature for a pulsing frequency of (a)  $1/20 \text{ Hz}$ , (b)  $1/10 \text{ Hz}$ , (c)  $1/3 \text{ Hz}$ , (d)  $1 \text{ Hz}$ . The average rate of  $\text{Ba}(\text{NO}_3)_2$  change during the storage phase is indicated by  $\alpha$ . Please note the time axes are blown up for Fig. 12c and d relative to Fig. 12a and b.

sample  $\beta$ . This led to the same number of PGM sites in both samples, but a larger average distance between sites in sample  $\beta$  due to dispersion of PGM sites in a larger volume of washcoat. In addition, because of the uniform distribution of barium in the washcoat, the number of  $\text{BaO}$  sites (i.e.,  $\text{NO}_x$  storage sites) was larger in sample  $\beta$  compared to sample  $\alpha$  in proportion to the volume of washcoat in the two samples. Fig. 13 is a SEM image of both samples. It should be noted again that due to higher washcoat thickness, the  $\text{NO}_x$  storage capacity of sample  $\beta$  was higher than sample  $\alpha$  and the average volumetric density of PGM sites of sample  $\beta$  was lower than sample  $\alpha$ .

Fig. 14 illustrates the cycle-averaged  $\text{NO}_x$  conversion efficiency of the RPR process using samples  $\alpha$  and  $\beta$  as a function of temperature at different pulsing frequencies, at 0.15 duty cycle and with inlet concentrations shown in Table 4. It is observed that at temperatures below  $450^\circ\text{C}$ , sample  $\beta$  demonstrates higher  $\text{NO}_x$  conversion which can be attributed to higher  $\text{NO}_x$  storage capacity. However, at temperatures

above  $450\text{--}500^\circ\text{C}$  with pulsing frequencies above  $0.05 \text{ Hz}$  (pulsing period lower than  $20 \text{ s}$ ), sample  $\alpha$  consistently outperforms sample  $\beta$ . Hypothetically, this can be attributed to increased washcoat mass transfer resistance in sample  $\beta$  which becomes the rate limiting step in some of the reactions of the RPR process.

### 6.1. Internal effectiveness factor

To gain insight into the underlying reason for the observations in Fig. 14, the developed model was employed to study the influence of washcoat mass transfer resistance. The washcoat geometries of samples were directly used to create a discretized computational domain as shown in Fig. 15. The effective diffusivity in the washcoat is obtained using Eq. (7) [26], where  $D_{AB}$  is the molecular diffusivity, and  $D_{KA}$  is the Knudsen diffusivity. The values of molecular diffusivity are calculated using the Hirschfelder relation, Eq. (8), and listed in Section S.3.2 of the Supporting information. In addition, the Knudsen diffusivity is obtained using Eq. (9), where  $d$  is the mean pore diameter of the washcoat which is measured using nitrogen physisorption, as described below.

$$\frac{1}{D_{Ae}} = \frac{1}{D_{AB}} + \frac{1}{D_{KA}} \quad (7)$$

$$D_{AB} = \frac{0.001858 T^{3/2} \left[ \frac{1}{M_A} + \frac{1}{M_B} \right]^{1/2}}{P \sigma_{AB}^2 \Omega_D} \quad (8)$$

$$D_{KA} = \frac{d}{3} \sqrt{\frac{8RT}{\pi M_A}} \quad (9)$$

The surface area and pore volume analysis of the washcoat was conducted using nitrogen physisorption (Micromeritics ASAP 2020). Using the nitrogen isotherm calculations based on the BET approach [34], a surface area of  $40.72 \text{ m}^2/\text{g}$  was obtained. In addition, the pore size distribution was calculated based on BJH desorption pore analysis and is shown in Fig. 16 with a peak at  $105 \text{ \AA}$  and a shoulder contribution at  $145 \text{ \AA}$ , with no macropores. This pore size distribution compares closely with the mean pore size value of  $100 \text{ \AA}$  ( $10 \text{ nm}$ ) used in the literature for automotive catalysis [35], which is also used in our model for calculation of Knudsen diffusivity (Eq. (9)).

The extent of washcoat mass transfer limitation can be quantified using an internal effectiveness factor,  $\phi$ , which is the ratio of actual reaction rate to the reaction rate that would result if the entire interior surface of the washcoat were exposed to the surface concentration [36]. Fig. 17 shows the effectiveness factor as a function of temperature for a number of important  $\text{NO}_x$  storage and surface/gas phase  $\text{NO}_x$  reduction reactions. Since the value of the effectiveness factor is dependent on the concentration of gas phase and surface species involved in each reaction, it is calculated in a range of relevant species concentrations that might occur during the rich/lean period of the RPR reaction (as explained in S.2 of the Supporting information) and the variation range of the effectiveness factor at each temperature is shown by the shaded bands in Fig. 17.

As can be seen in Fig. 17, in all the reactions a thicker washcoat has a lower value of effectiveness factor, an indication of more internal mass transfer limitation. First, let us consider the primary  $\text{NO}_x$  storage reaction, RXN12, which indicates large values of effectiveness factor, above  $0.8$  across the entire temperature range, which indicates that this reaction is not limited by internal mass transfer. Now let us consider different surface  $\text{NO}_x$  reduction reactions. The surface  $\text{NO}_x$  reduction with  $\text{H}_2$  (RXN 15) and with  $\text{CO}$  (RXN 14) which have large diffusivities, indicate large values of effectiveness factor across the entire range (note varying y-axis scales in the figure), and therefore are not limited by internal mass transfer. However, the steam reforming reaction, RXN 7, which is the primary path for generation of  $\text{CO}$  and  $\text{H}_2$  is moderately limited at high temperatures specifically for a thicker washcoat, limiting the formation of these reductants for  $\text{NO}_x$  reduction. The direct



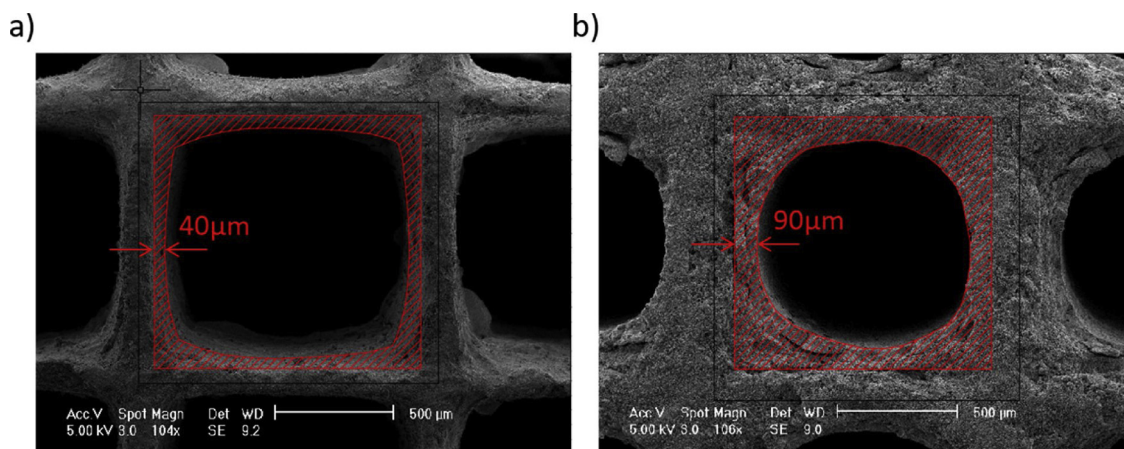


**Fig. 13.** Cross section SEM images of two control samples for mass transfer experiments. Both having identical washcoat composition and loading of PGM, (a) low washcoat thickness (sample  $\alpha$ ), (b) high washcoat thickness (sample  $\beta$ ).

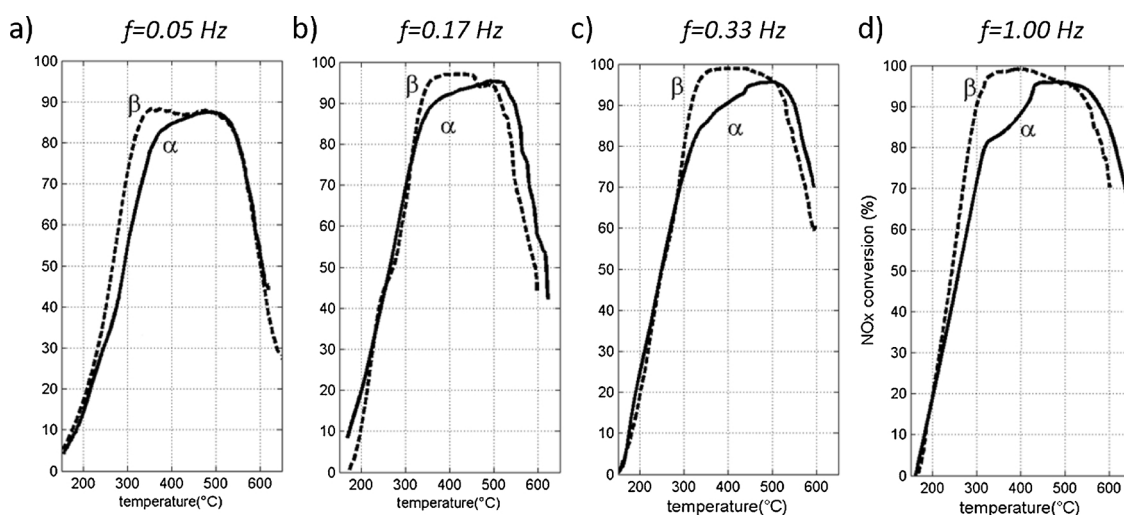


**Fig. 14.** Cycle-averaged NO<sub>x</sub> conversion efficiency of the RPR process using two samples  $\alpha$  and  $\beta$  (samples shown in Fig. 13) at pulsing frequencies of a) 0.05 Hz, b) 0.17 Hz, c) 0.33 Hz, and d) 1.00 Hz.

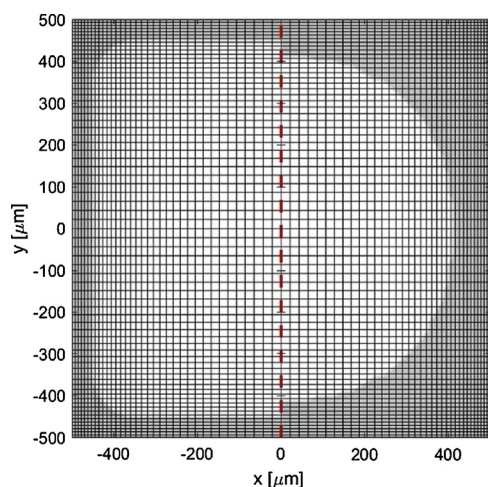


**Fig. 15.** Computational domain of a monolith channel, the lighter central region indicates the gas phase and the darker region indicates the porous solid washcoat. The left half shows a thinner washcoat (sample  $\alpha$ ), and the right half shows a thicker washcoat (sample  $\beta$ ).

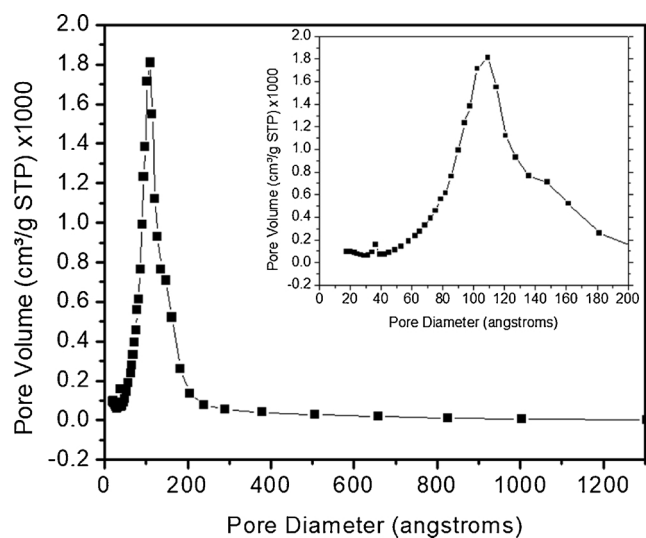


**Fig. 16.** Pore size distribution of LNT washcoat obtained using BJH desorption. The subset shows a main peak at 105 Å and a shoulder contribution at 145 Å.



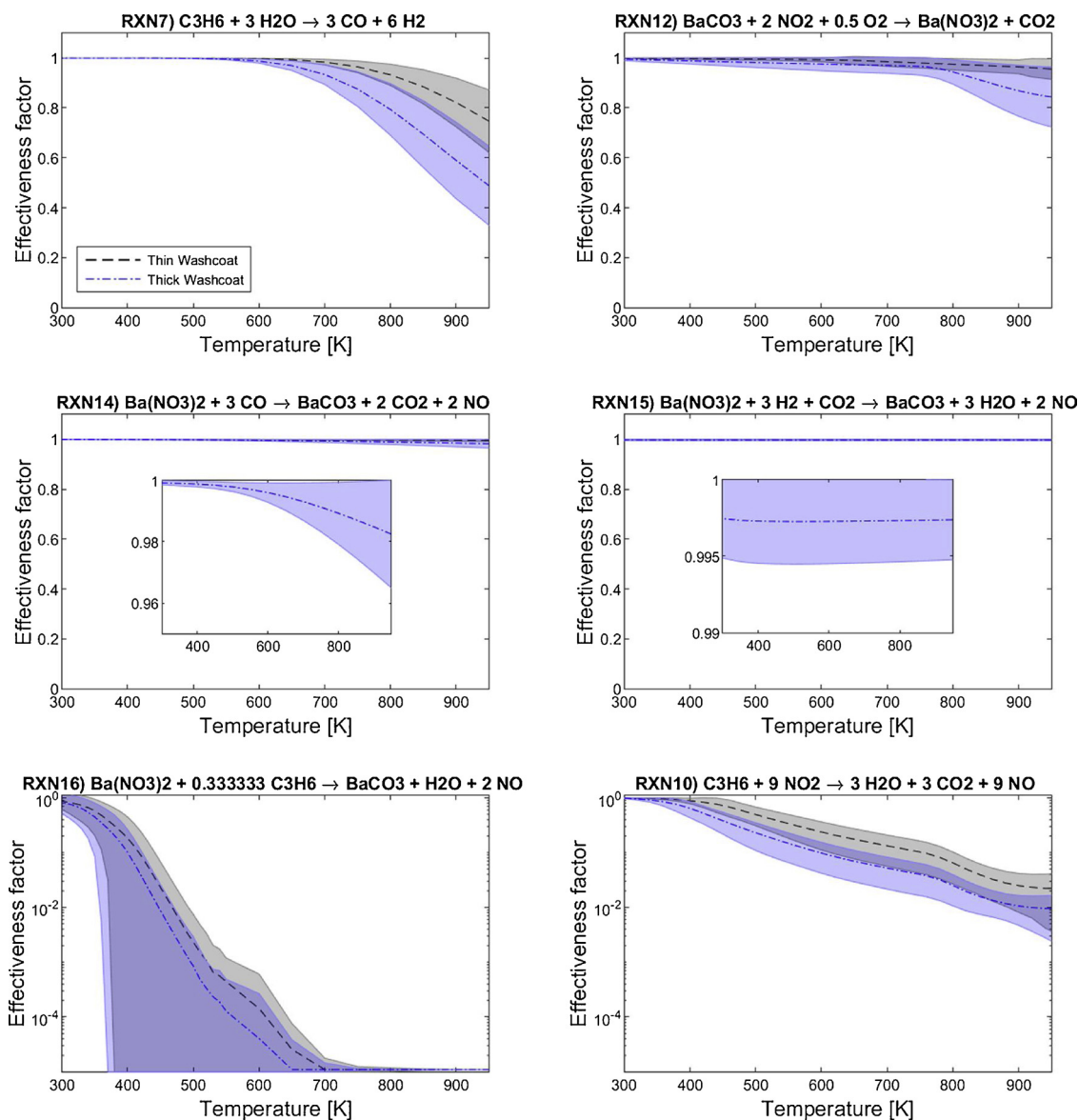


**Fig. 17.** Effectiveness factor as a function of temperature for two washcoat geometries. Black: thin washcoat (40  $\mu\text{m}$ ) and blue: thick washcoat (90  $\mu\text{m}$ ), samples shown in Fig. 13. For reactions (a) 7, (b) 10, (c) 12, (d) 14, (e) 15, and (f) 16 as listed in Table 1. The dashed lines indicate the mean of the effectiveness factor and the shaded bands indicate the range of its variation at each temperature as the inlet concentration of species is changed in a range relevant to the RPR reaction. The insets in (c) and (d) show the effectiveness factor with an expanded y-axis range, since these reactions are not limited by internal mass transfer. Note that the y-axes in (e) and (f) are logarithmic, while the rest are linear (For interpretation of the references to colour in this figure legend, the reader is referred to the web version of this article).

reduction of surface and gas phase NO<sub>x</sub> with propylene, RXN 16 and 10, are significantly limited by mass transfer. In both reactions, the thicker washcoat shows an effectiveness factor value significantly smaller than the thinner washcoat. These modeling results indicate that the NO<sub>x</sub> reduction step, either directly by propylene, or by CO and H<sub>2</sub> formed from the steam reforming pathway, is limited by mass transfer especially at higher temperatures, and the extent of limitation is dependent on the washcoat thickness. This mass transfer limitation is specifically important at higher pulsing frequencies, where the pulses become smeared out due to mixing and the concentration gradient which is the driving force for mass transport becomes increasingly limited. Therefore, the model results suggest that the poor performance of a thicker washcoat at high frequencies/temperatures, as shown in Fig. 14, is a result of mass transfer limitations on the NO<sub>x</sub> reduction step.

## 7. Conclusions

A global kinetic model was developed to model the RPR process with propylene as the injected reductant at temperatures  $\geq 450$  °C. The model includes PGM, barium and cerium sites with 23 reactions including oxidation, water gas shift, steam reforming, NO<sub>x</sub> storage, gas phase and stored NO<sub>x</sub> reduction, ammonia formation, and oxygen storage/reduction. The model parameters were tuned to fit low-frequency lean/rich switching experiments with a wide range of temperatures and feed gas compositions. The same model parameters were used to explore the high frequency behavior of the RPR process and was able to accurately predict the improvement in cycle-averaged NO<sub>x</sub> conversion and transient product traces as the pulsing frequency was increased from a typical LNT frequency ( $\sim 0.01$  Hz) to an optimal RPR frequency ( $\sim 1$  Hz).

It should be mentioned that since the model reactions and parameters were completely based on conventional “low frequency” LNT

operation and did not include any hydrocarbon or isocyanate intermediates on the surface, the improvement in NO<sub>x</sub> conversion at high pulsing frequencies/temperatures using hydrocarbon reductants can be primarily explained by conventional LNT models. The model indicated that the required NO<sub>x</sub> storage capacity decreases and the cycle-averaged rate of NO<sub>x</sub> storage step increases at higher pulsing frequencies, which leads to a higher overall NO<sub>x</sub> conversion at high temperatures where the NO<sub>x</sub> storage capacity becomes significantly limited.

However, the global kinetic model described above was not able to predict the decline in NO<sub>x</sub> conversion, nor the significant decrease in reaction products such as NH<sub>3</sub> and CO as the pulsing frequency was increased past the optimal RPR frequency (i.e., high frequency regime  $f \geq 1$  Hz). It was necessary to include reductant pulse mixing effects upstream of the catalyst in order to predict the RPR behavior in the high-frequency regime, and predict the general reducing trend of reaction product concentrations, which indicates the importance of pulse mixing in achieving high RPR performance.

In addition, this model was employed to study the effects of washcoat mass transfer limitations, which have been shown experimentally to limit the NO<sub>x</sub> conversion at high temperatures and frequencies above 1/6 Hz. Calculations of the internal effectiveness factor for two different washcoat geometries with identical formulations, but different washcoat thicknesses, indicated that washcoat diffusion becomes the rate limiting step for stored NO<sub>x</sub> reduction with propylene.

Overall, a kinetics + pulse mixing model is capable of accurately predicting the NO<sub>x</sub> conversion of the RPR process over the wide frequency range of  $\sim 0.01$  Hz to  $\sim 10$  Hz, and there is no need for inclusion of stable surface intermediates for predicting RPR performance. However, the selectivity of reaction products is not accurately obtained here and only the trends vs. frequency are well predicted. To better predict the product selectivity an independent tuning of the model and/or inclusion of a more detailed reaction mechanism is required.

## Acknowledgments

The University of Michigan authors acknowledge the Ford Motor Company within the UM-Ford Alliance Program for its encouragement and support of the experimental work that motivated this modeling work. We also gratefully thank Dr. Jason Gaudet of UM for his determination of the pore size distribution of our catalyst samples. And we thank Dr. Chang Yup Seo for taking the SEM micrographs of our samples and acknowledge the University of Michigan Center for Materials Characterization for the use of its instruments and the assistance of its staff.

## Appendix A. Supplementary data

Supplementary material related to this article can be found, in the online version, at doi:<https://doi.org/10.1016/j.apcatb.2019.04.076>.

## References

- [1] Y. Bisaiji, K. Yoshida, M. Inoue, K. Umemoto, T. Fukuma, Development of di-air – a new diesel deNO<sub>x</sub> system by adsorbed intermediate reductants, SAE Pap. 5 (2011) 678–686, <https://doi.org/10.4271/2011-01-2089>.
- [2] C.C.Y. Perng, V.G. Easterling, M.P. Harold, Fast lean-rich cycling for enhanced NO<sub>x</sub> conversion on storage and reduction catalysts, Catal. Today 231 (2014) 125–134, <https://doi.org/10.1016/j.cattod.2014.01.026>.
- [3] A. Reihani, G.B. Fisher, J.W. Hoard, J.R. Theis, J.D. Pakko, C.K. Lambert, Rapidly pulsed reductants for diesel NO<sub>x</sub> reduction with lean NO<sub>x</sub> traps: effects of pulsing parameters on performance, Appl. Catal. B Environ. 223 (2018) 177–191, <https://doi.org/10.1016/j.apcatb.2017.07.054>.
- [4] J.B. Heywood, Internal Combustion Engine Fundamentals, McGraw-Hill, New York, 1988.
- [5] T.V. Johnson, CE-2016-306 directions in vehicle efficiency and emissions, Combust. Engines 166 (2017) 3–8, <https://doi.org/10.19206/CE-2016-306>.
- [6] T.V. Johnson, A. Joshi, Review of deNO<sub>x</sub> Technology for Mobile Applications, (2018), <https://doi.org/10.1039/9781788013239-FP009>.
- [7] T.V. Johnson, Review of vehicular emissions trends, SAE Int. J. Engines 8 (2015), <https://doi.org/10.4271/2015-01-0993>.
- [8] Y. Li, S. Roth, J. Dettling, T. Beutel, Effects of lean / rich timing and nature of

- reductant on the performance of a NO<sub>x</sub> trap catalyst, Top. Catal. 16 (17) (2001) 139–144, <https://doi.org/10.1023/a:1016651418882>.
- [10] J.S. Hepburn, E. Thanasiu, D.A. Dobson, W.L. Watkins, Experimental and Modeling Investigations of NO<sub>x</sub> Trap Performance 962051 Experimental and Modeling Investigations of NO<sub>x</sub> Trap Performance, (1996), <https://doi.org/10.4271/962051>.
- [11] M. Inoue, Y. Bisaiji, K. Yoshida, deNO<sub>x</sub> Performance and Reaction Mechanism of the Di-Air System, (2013), pp. 3–6, <https://doi.org/10.1007/s11244-013-9919-2>.
- [12] A. Reihani, B. Patterson, J. Hoard, G.B. Fisher, J.R. Theis, C.K. Lambert, Rapidly pulsed reductants for diesel NO<sub>x</sub> reduction with lean NO<sub>x</sub> traps: comparison of alkanes and alkenes as the reducing agent, J. Eng. Gas Turbines Power 139 (2017) 102805.
- [13] A.W.L. Ting, M.P. Harold, V. Balakotaiah, Elucidating the mechanism of fast cycling NO<sub>x</sub> storage and reduction using C<sub>3</sub>H<sub>6</sub> and H<sub>2</sub> as reductants, Chem. Eng. Sci. 189 (2018) 413–421, <https://doi.org/10.1016/j.ces.2018.05.021>.
- [14] A. Reihani, B. Corson, J.W. Hoard, G.B. Fisher, E. Smirnov, D. Roemer, J. Theis, C. Lambert, Rapidly pulsed reductants in diesel NO<sub>x</sub> reduction by lean NO<sub>x</sub> traps: effects of mixing uniformity and reductant type, SAE Int. J. Engines 9 (2016), <https://doi.org/10.4271/2016-01-0956> 2016-01-0956.
- [15] L. Olsson, R.J. Blint, E. Fridell, Global kinetic model for lean NO<sub>x</sub> traps, Ind. Eng. Chem. Res. 44 (2005) 3021–3032, <https://doi.org/10.1021/ie0494059>.
- [16] P. Kočí, M. Schejbal, J. Trdlička, T. Gregor, M. Kubíček, M. Marek, Transient behaviour of catalytic monolith with NO<sub>x</sub> storage capacity, Catal. Today 119 (2007) 64–72, <https://doi.org/10.1016/j.cattod.2006.08.014>.
- [17] P. Kočí, F. Plát, J. Štěpánek, Š. Bártová, M. Marek, M. Kubíček, V. Schmeißer, D. Chatterjee, M. Weibel, Global kinetic model for the regeneration of NO<sub>x</sub> storage catalyst with CO, H<sub>2</sub> and C<sub>3</sub>H<sub>6</sub> in the presence of CO<sub>2</sub> and H<sub>2</sub>O, Catal. Today 147 (2009), <https://doi.org/10.1016/j.cattod.2009.07.036>.
- [18] R.S. Larson, J.A. Pihl, V. Kalyana Chakravarthy, T.J. Toops, C.S. Daw, Microkinetic modeling of lean NO<sub>x</sub> trap chemistry under reducing conditions, Catal. Today 136 (2008) 104–120, <https://doi.org/10.1016/j.cattod.2007.12.117>.
- [19] C. Shi, Y. Ji, U.M. Graham, G. Jacobs, M. Crocker, Z. Zhang, Y. Wang, T.J. Toops, NO<sub>x</sub> storage and reduction properties of model ceria-based lean NO<sub>x</sub> trap catalysts, Appl. Catal. B Environ. 119–120 (2012) 183–196, <https://doi.org/10.1016/j.apcatb.2012.02.028>.
- [20] J.A. Pihl, J.A. Lewis, T.J. Toops, J.E. Parks, Lean NO<sub>x</sub> trap chemistry under lean-gasoline exhaust conditions: impact of high NO<sub>x</sub> concentrations and high temperature, Top. Catal. 56 (2013) 89–93, <https://doi.org/10.1007/s11244-013-9934-3>.
- [21] J. Xu, R. Clayton, V. Balakotaiah, M.P. Harold, Experimental and microkinetic modeling of steady-state NO reduction by H<sub>2</sub> on Pt/BaO/Al<sub>2</sub>O<sub>3</sub> monolith catalysts, Appl. Catal. B Environ. 77 (2008) 395–408, <https://doi.org/10.1016/j.apcatb.2007.08.008>.
- [22] A.W.L. Ting, M. Li, M.P. Harold, V. Balakotaiah, Fast cycling in a non-isothermal monolithic lean NO<sub>x</sub> trap using H<sub>2</sub> as reductant: experiments and modeling, Chem. Eng. J. 326 (2017) 419–435, <https://doi.org/10.1016/j.cej.2017.05.002>.
- [23] C. Depcik, D. Assanis, K. Bevan, A one-dimensional lean NO<sub>x</sub> trap model with a global kinetic mechanism that includes NH<sub>3</sub> and N<sub>2</sub>O, Int. J. Engine Res. 9 (2008) 57–77, <https://doi.org/10.1243/14680874JERO1807>.
- [24] E. Ozensoy, C.H.F. Peden, J. Szanyi, Model NO<sub>x</sub> storage systems: storage capacity and thermal aging of BaO/θ-Al<sub>2</sub>O<sub>3</sub>/NiAl(100), J. Catal. 243 (2006) 149–157, <https://doi.org/10.1016/j.jcat.2006.06.028>.
- [25] F.M. White, Fluid Mechanics, McGraw Hill, New York, 2011.
- [26] R.B. Bird, Transport phenomena, Appl. Mech. Rev. 55 (2002) R1–R4.
- [27] J. Chen, H. Yang, N. Wang, Z. Ring, T. Dabros, Mathematical modeling of monolith catalysts and reactors for gas phase reactions, Appl. Catal. A Gen. 345 (2008) 1–11.
- [28] J.L. Devore, Probability and Statistics for Engineering and the Sciences, Cengage Learning, 2011.
- [29] D. Mráček, P. Kočí, M. Marek, J.S. Choi, J.A. Pihl, W.P. Partridge, Dynamics of N<sub>2</sub> and N<sub>2</sub>O peaks during and after the regeneration of lean NO<sub>x</sub> trap, Appl. Catal. B Environ. 166–167 (2015) 509–517, <https://doi.org/10.1016/j.apcatb.2014.12.002>.
- [30] L. Lietti, I. Nova, P. Forzatti, Role of ammonia in the reduction by hydrogen of NO<sub>x</sub> stored over Pt-Ba/Al<sub>2</sub>O<sub>3</sub> lean NO<sub>x</sub> trap catalysts, J. Catal. 257 (2008) 270–282, <https://doi.org/10.1016/j.jcat.2008.05.005>.
- [31] C.D. DiGiulio, J.A. Pihl, J.S. Choi, J.E. Parks, M.J. Lance, T.J. Toops, M.D. Amiridis, NH<sub>3</sub> formation over a lean NO<sub>x</sub> trap (LNT) system: effects of lean/rich cycle timing and temperature, Appl. Catal. B Environ. 147 (2014) 698–710, <https://doi.org/10.1016/j.apcatb.2013.09.012>.
- [32] V. Easterling, Y. Ji, M. Crocker, M. Dearth, R.W. McCabe, Application of spaciMS to the study of ammonia formation in lean NO<sub>x</sub> trap catalysts, Appl. Catal. B Environ. 123–124 (2012) 339–350, <https://doi.org/10.1016/j.apcatb.2012.05.002>.
- [33] S.Y. Joshi, M.P. Harold, V. Balakotaiah, Overall mass transfer coefficients and controlling regimes in catalytic monoliths, Chem. Eng. Sci. 65 (2010) 1729–1747, <https://doi.org/10.1016/j.ces.2009.11.021>.
- [34] S. Brunauer, P.H. Emmett, E. Teller, Adsorption of gases in multimolecular layers, J. Am. Chem. Soc. 60 (1938) 309–319.
- [35] T. Starý, O. Šolcová, P. Schneider, M. Marek, Effective diffusivities and pore-transport characteristics of washcoated ceramic monolith for automotive catalytic converter, Chem. Eng. Sci. 61 (2006) 5934–5943, <https://doi.org/10.1016/j.ces.2006.05.014>.
- [36] H.S. Fogler, Essentials of Chemical Reaction Engineering, Pearson Education, Upper Saddle River N.J., 2010.

## Further reading

- [2] Y. Bisaiji, K. Yoshida, M. Inoue, N. Takagi, T. Fukuma, Reaction mechanism analysis of di-air-contributions of hydrocarbons and intermediates, SAE Int. J. Fuels Lubr. 5 (2012) 1310–1316, <https://doi.org/10.4271/2012-01-1744>.